

# X-ray studies of the gamma-ray pulsar J1826–1256 and its pulsar wind nebula with *Chandra* and XMM-*Newton*

Anna V. Karpova<sup>1★</sup>, Dmitry A. Zyuzin<sup>1†</sup> and Yuriy A. Shibano<sup>1</sup>

<sup>1</sup>*Ioffe Institute, Politekhnikeskaya 26, St. Petersburg, 194021, Russia*

Accepted XXX. Received YYY; in original form ZZZ

## ABSTRACT

We have analyzed archival XMM-*Newton* and *Chandra* observations of the  $\gamma$ -ray radio-quiet pulsar J1826–1256 and its pulsar wind nebula. The pulsar spectrum can be described by a power-law model with a photon index  $\Gamma \approx 1$ . We find that the nebular spectrum softens with increasing distance from the pulsar, implying synchrotron cooling. The empirical interstellar absorption–distance relation gives a distance of  $\approx 3.5$  kpc to J1826–1256. We also discuss the nebula geometry and association between the pulsar, the very high energy source HESS J1826–130, the supernova remnant candidate G18.45–0.42 and the open star cluster Bica 3.

**Key words:** stars: neutron – pulsars: general – pulsars: individual: PSR J1826–1256

## 1 INTRODUCTION

The *Fermi* observatory opened a new window in the studies of  $\gamma$ -ray emission from compact objects. To date, the Large Area Telescope (LAT) onboard *Fermi* has detected more than 200 rotation powered pulsars<sup>1</sup>. Multiwavelength observations of pulsars allow researchers to study the pulsar emission geometry, particle acceleration mechanisms in the pulsar magnetosphere and pulsar emission efficiencies as a function of energy (e.g. Takata & Cheng 2017). They are also important for investigation of the thermal emission from pulsar surfaces (e.g. Kargaltsev & Pavlov 2007). Since more than a quarter of *Fermi* pulsars is radio-quiet, X-ray observations play a key role in understanding their properties (e.g. Marelli et al. 2013, 2015). Investigations in this band can reveal their pulsar wind nebulae (PWNe) and associated supernova remnants (SNRs). Studies of the latter objects, in turn, provide additional information about pulsar parameters (e.g. ages, distances, proper motions, geometries) and interaction of relativistic pulsar winds with the ambient medium (e.g., Gaensler & Slane 2006; Kargaltsev et al. 2017).

The young and energetic radio-quiet PSR J1826–1256 was one of the first pulsars discovered in  $\gamma$ -rays using blind frequency searches in *Fermi* data (Abdo et al. 2009). This is one of the brightest radio-quiet  $\gamma$ -ray pulsars listed in the last *Fermi* catalog (3FGL J1826.1–1256; Acero et al. 2015). It has a period  $P = 110.2$  ms, a spin-down luminosity  $\dot{E} = 3.6 \times 10^{36}$  erg s<sup>-1</sup>, a characteristic age  $\tau_c = 14$  kyr and a

surface magnetic field  $B = 3.7 \times 10^{12}$  G. Judging by these parameters the pulsar belongs to a group of ‘Vela-like’ pulsars. The distance (‘pseudo’-distance) to PSR J1826–1256 was estimated to be  $\sim 1.2$  kpc (Marelli 2012) using the empirical relation between the distance and the  $\gamma$ -ray flux above 100 MeV (Saz Parkinson et al. 2010). This estimate is known to be very uncertain. Ray et al. (2011) performed precise  $\gamma$ -ray timing analysis improving the accuracy of the pulsar’s *Fermi* position. Its coincidence with an X-ray point-like source previously detected with *Chandra* (Roberts et al. 2007) implied that the latter is the PSR J1826–1256 counterpart. Detection in the XMM-*Newton* data of X-ray pulsations with the pulsar period from the point source (Li et al. 2018) confirmed its pulsar nature. Analyzing *Chandra* data, Marelli (2012) showed that PSR J1826–1256 has a flat X-ray spectrum described by a power law (PL) with the photon index  $\Gamma = 0.79 \pm 0.39$ .

Before the pulsar’s discovery, the *Advanced Satellite for Cosmology and Astrophysics* (*ASCA*) observatory revealed a  $\sim 15$  arcmin X-ray nebula AX J1826.1–1300, presumably a PWN, detected within the error-box of a bright previously unidentified  $\gamma$ -ray source 3EG J1826–1302 (Roberts et al. 2001). Observations with *Chandra* (Roberts et al. 2007) resolved in the nebula beside the pulsar, a faint, remarkably long trail-like PWN (G18.5–0.4) and a stellar cluster Bica 3<sup>2</sup>. G18.5–0.4 is connected to the pulsar and extended by  $\sim 4$  arcmin south-west from it. Owing to its shape, it was referred to as the Eel nebula (Roberts et al. 2007). Marelli

★ E-mail: annakarpova1989@gmail.com

† E-mail: da.zyuzin@gmail.com

<sup>1</sup> <https://confluence.slac.stanford.edu/display/GLAMCOG/Public+List+of+XMM-Newton+Gamma-Ray+Pulsars/all/openclust.html>

<sup>2</sup> Bica 3 can be found in the New Optically Visible Open Clusters and Candidates Catalog (OPENCLUST; Dias et al. 2002);

(2012) found that its X-ray emission extracted within 20 arcsec from the pulsar has a PL spectrum with  $\Gamma = 0.86 \pm 0.39$ , which is marginally steeper than that of PSR J1826–1256. Roberts et al. (2007) also noted, that there is a 90 cm radio emission, which may be related to the Eel by its morphology, and the absence of associated mid-infrared emission implies a non-thermal origin. Using *Fermi* data, Ackermann et al. (2011) performed the maximum likelihood spectral fits for the PSR J1826–1256 off-pulse emission and did not find any signature of the PWN in the GeV range.

At the same time, Eel together with PSR J1826–1256 overlap with the extended TeV source HESS J1826–130 which was previously considered to be a part of the brighter TeV PWN HESS J1825–137 (Angüner et al. 2017; H.E.S.S. Collaboration et al. 2018). The source has a very hard spectrum similar to that of the Vela X PWN, which can be produced by uncooled electrons with the spectral index close to 2.0 and a cut-off energy at around 70 TeV generated by the PSR+PWN system (Angüner et al. 2017). The TeV source was proposed to be associated with the Eel (Roberts et al. 2007), although a firm conclusion was not possible, in part due to the uncertainty of the distance to the pulsar (H.E.S.S. Collaboration et al. 2018).

HESS J1826–130 also partially overlaps with the SNR G18.6–0.2 (Brogan et al. 2006) which may indicate their association (H.E.S.S. Collaboration et al. 2018). However, the latter is unlikely since this SNR has a significantly smaller size and a large offset from the TeV source center.

In the radio and mid-infrared, Anderson et al. (2017) detected a shell-like SNR candidate G18.45–0.42. We found that its position and size are well compatible with the Eel and HESS J1826–130, making its association with these objects possible.

Here we report the simultaneous X-ray analysis of archival XMM-*Newton* and *Chandra* observations of PSR J1826–1256 and its PWN. The details of observations and imaging are described in Section 2. The spectral analysis is presented in Section 3. We discuss the results in Section 4. Based on the interstellar absorption versus distance relation we obtain a new distance estimation to the PSR+PWN system of  $\approx 3.5$  kpc. We consider G18.45–0.42 as the best SNR candidate for possible association with the PSR J1826–1256 and its PWN. The summary is given in Section 5.

## 2 X-RAY DATA AND IMAGING

A 140 ks XMM-*Newton* observation of PSR J1826–1256 field was carried out on 2014 October 11 (ObsID 0744420101, PI Razzano). European Photon Imaging Camera Metal Oxide Semiconductor (EPIC-MOS) data were obtained in the Full Frame mode using the medium optical filter, while the EPIC-pn camera was operated in the Small Window mode with the thin optical filter<sup>3</sup>. We also used *Chandra* Advanced CCD Imaging Spectrometer (ACIS-I) observations performed on 2003 February 17 (ObsID 3851, PI Romani, exposure time 15.1 ks, off-axis observation) and on 2007 July 26 (ObsID 7641, PI Roberts, exposure time 74.8 ks). We

used the XMM-SAS v.16.0.0 and CIAO v.4.9 tools to reduce the data.

The *Chandra* data were reprocessed using the CHANDRA\_REPRO tool. In the top left panel of Fig. 1 we show the field of view (FoV) of the ACIS-I<sup>4</sup> detector in the 0.5–10 keV band created by the CIAO FLUXIMAGE tool from the longest *Chandra* dataset (ObsID 7641). The ‘+’ symbol marks the pulsar position (RA = 18<sup>h</sup>26<sup>m</sup>08<sup>s</sup>.56, Dec = –12°56′34″.9) obtained using the WAVDETECT tool. The Eel trail extending south-west from PSR J1826–1256 and a fainter diffuse emission from the rest south part of the PWN are seen, along with brighter emission from the open star cluster Bica 3.

The XMM-*Newton* data were reduced by the EMCHAIN and EPCHAIN tools and periods of background flares were excluded by the ESPFILT task with default parameters for the pn data and the MOS-FILTER command for the MOS data (the latter also runs ESPFILT). The resulting exposures are 77.5, 81.2 and 49.8 ks for MOS1, MOS2 and pn, respectively. The EPIC-pn FoV in the 0.5–10 keV band is shown in the top right panel of Fig. 1. Since this camera was operated in the Small Window mode, it does not cover the whole PWN. For comparison, its FoV is shown in the *Chandra* image.

To obtain a wider and deeper image of the pulsar field, we combined data from both MOS detectors. To do this, we utilize the XMM-*Newton* Extended Source Analysis Software (ESAS; Snowden & Kuntz 2014). The MOS images and exposure maps were generated by MOS-SPECTRA tool (MOS1 CCDs 3 and 6 are no longer used, since they have been damaged by micrometeorites). Quiescent particle background (QPB) images were created by the MOS\_BACK task. Then MOS QPB-background subtracted and exposure corrected images were combined and adaptively smoothed by the ADAPT tool using 150 counts for the smoothing kernel. The resulting image in the 0.5–10 keV band is shown in the bottom left panel of Fig. 1. This is the deepest up-to-date soft X-ray image of the pulsar field. The PWN emission, as well as the open star cluster Bica 3, is more visible than in the ACIS image. Positions and extents of SNR candidate G18.45–0.42, HESS J1826–130 and SNR G18.6–0.2 are shown by circles. The former two strongly overlap with each other and with the X-ray PWN, indicating their possible association, as has been mentioned in Section 1, while the latter one has a large angular distance offset, suggesting that it is an unrelated object.

To reveal the nebula emission better, we removed point-like sources detected by the CHEESE task in the XMM-*Newton* data and by the WAVDETECT command in the *Chandra* datasets. We refilled the resulting holes with values of the surrounding background emission using the CIAO DM-FILTH tool. The exclusion of PSR J1826–1256 distorts the shape of the PWN so it was not removed. The resulting image smoothed using the smoothing kernel of 150 counts is presented in the bottom right panel of Fig. 1. In the XMM-*Newton* data, the Eel trail is detected up to 6 arcmin from the pulsar, while in the less-sensitive *Chandra* observations only up to 4 arcmin. Fainter diffusive nebula emission in the south may be somewhat blended with Bica 3. Overall, the nebula resembles a cometary-like tail behind

<sup>3</sup> <https://www.cosmos.esa.int/web/xmm-newton/technical-details-4><sup>4</sup><http://asc.harvard.edu/proposer/POG/html/chap6.html>

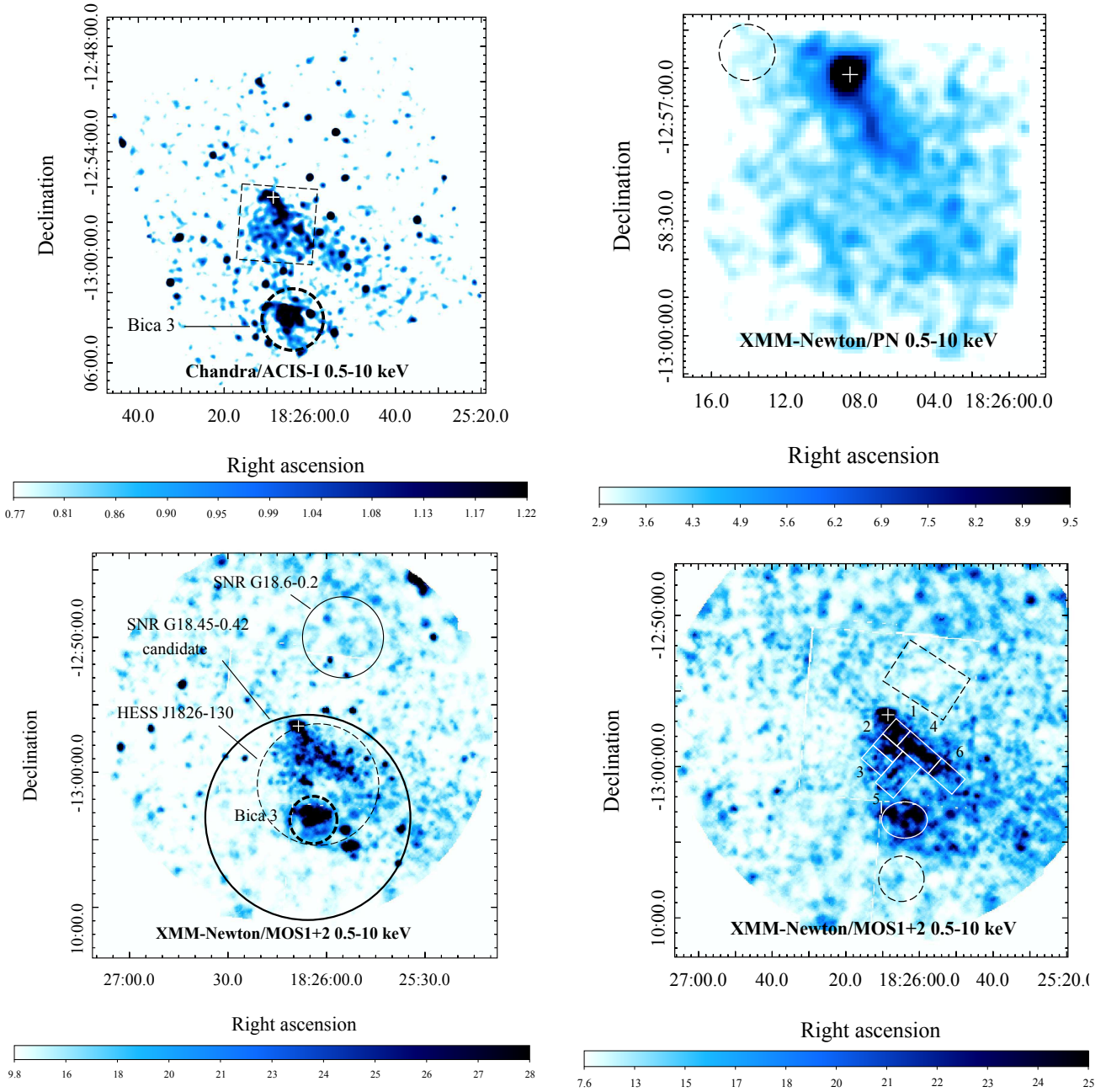


**Figure 1.** 0.5–10 keV images of the PSR J1826–1256 field. The pulsar *Chandra* position is shown by the ‘+’ symbol. *Top left:* Exposure-corrected FoV of the *Chandra* ACIS-I detector. The intensity is given in  $10^{-8}$  ph cm $^{-2}$  s $^{-1}$  pixel $^{-1}$ . The black dashed box shows the EPIC-pn FoV. The open star cluster Bica 3 is marked. *Top right:* FoV of the XMM-Newton EPIC-pn camera in Small Window mode. The dashed circle shows the background region for the pulsar spectral analysis. The intensity is given in counts pixel $^{-1}$ . *Bottom:* Combined XMM-Newton MOS1 and MOS2 exposure-corrected QPB-subtracted images. In the bottom left panel bold solid, bold dashed, thin dashed and thin solid circles indicate the positions and extents of the SNR candidate G18.45–0.42, open cluster Bica 3, HESS J1826–130 and SNR G18.6–0.2, respectively (HESS J1826–130 has the size of 0.15 deg which is  $1\sigma$  for a single-Gaussian spatial model; H.E.S.S. Collaboration et al. 2018). In the bottom right panel we removed point sources except PSR J1826–1256. Rectangular regions used for the PWN spectral analysis are shown and numbered in order of their distance from the pulsar. The dashed polygon was used for the background. The ellipse and circle show regions used to extract spectra of Bica 3 and corresponding background, respectively. The intensity is given in counts s $^{-1}$  deg $^{-2}$ .

PSR J1826–1256 which is typical for PWNe created by fast-moving pulsars (Kargaltsev et al. 2017).

### 3 SPECTRAL ANALYSIS

To perform pulsar spectral analysis, we extracted spectra from MOS and pn data using the EVSELECT tool and the 15-arcsecs radius circle around the PSR J1826–1256

*Chandra* position<sup>5</sup>. For the background, we used the region free from any sources (top right panel of Fig. 1). The RMFGEN and ARFGEN tasks were applied to generate the redistribution matrix and ancillary response files. The spectra were grouped to ensure 20 counts per energy bin. We also extracted the PSR J1826–1256 spectrum from the longest *Chandra*/ACIS-I dataset utilizing the CIAO SPECEXTARCT tool and the 2-arcsecs radius circle (the short off-axis *Chandra* observation provides much smaller number of counts and was neglected). It was also grouped to ensure 20 counts per energy bin. We obtained 352(MOS1)+383(MOS2)+739(pn)+207(ACIS) source counts in the 0.5–10 keV band. The XMM-*Newton* spectra contains both the pulsar and the adjacent PWN emission, due to the broad wings of the XMM-*Newton* point spread function (PSF). Thus, we generated the response files for a point source as well as for an extended source. To constrain the PWN contribution in the XMM-*Newton* spectra, we extracted its spectrum from the *Chandra* data using an annulus with inner and outer radii of 2.5 and 15 arcsec. This resulted in 206 source counts which were grouped to ensure 20 counts per energy bin. To analyse the PSR J1826–1256 spectra, we tried two different models: a power-law (PL) model which describes non-thermal magnetosphere emission and a black body (BB) model which describes thermal emission from the pulsar surface. The pulsar model was convolved with the response files for a point source. The PWN contribution was described by the PL model convolved with the response files for an extended source. We added a constant factor in the models, which represents the relative normalization between *Chandra* and XMM-*Newton* detectors.

To perform spatial-resolved spectral analysis of the Eel nebula at a larger scale, we extracted source and background spectra from the MOS data using regions shown and numbered in the right panel of Fig. 16. Point sources were excluded from these regions. The spectra of the regions were grouped to ensure 30 counts per energy bin and were analysed using PL models.

All spectra (including the pulsar, the adjacent PWN, i.e. within 15 arcsec from the pulsar and its more distant regions) were fitted simultaneously in the 0.5–10 keV band using XSPEC v.12.9.1 and assuming a common value of the absorption column density  $N_{\text{H}}$ . For photoelectric absorption, the XSPEC Tuebingen-Boulder interstellar medium (ISM) absorption model TBABS with the WILM abundances (Wilms et al. 2000) was used. We found that both PL and BB models chosen for the pulsar can describe its spectra well. However, the BB model resulted in temperature  $T \approx 1.4$  keV which is too large for pulsar thermal emission either from the whole stellar surface or a polar cap (see e.g. Viganò et al. 2013). Thus, we rejected this model. The resulting best-fitting parameters are presented in Tables 1 and 2. We obtained  $\chi^2 = 511$  for 549 degrees of freedom (d.o.f.). The spectra of the pulsar and the adjacent PWN are shown

**Table 1.** Best-fitting parameters for PSR J1826–1256 and adjacent PWN (i.e. within 15 arcsec from the pulsar) emission. All errors are at 90% confidence. Unabsorbed fluxes  $F_{\text{X}}$  in the 0.5–10 keV band were calculated using XSPEC convolution model CFLUX.  $N_{\text{bins}}$  = number of spectral bins. The cross-normalization constant was fixed at 1 for XMM-*Newton* spectra and free for *Chandra* spectra.

Column density $N_{\text{H}}$ , $10^{22}$ cm $^{-2}$	$2.2^{+0.2}_{-0.2}$
Pulsar photon index $\Gamma^{\text{psr}}$	$0.92^{+0.25}_{-0.24}$
Pulsar flux $F_{\text{X}}^{\text{psr}}$ , $10^{-13}$ erg s $^{-1}$ cm $^{-2}$	$1.04^{+0.14}_{-0.13}$
PWN photon index $\Gamma^{\text{pwn}}$	$1.20^{+0.24}_{-0.23}$
PWN flux $F_{\text{X}}^{\text{pwn}}$ , $10^{-13}$ erg s $^{-1}$ cm $^{-2}$	$0.85^{+0.10}_{-0.09}$
Cross-normalization constant	$1.14 \pm 0.13$
$\chi^2(N_{\text{bins}})$	94(114)

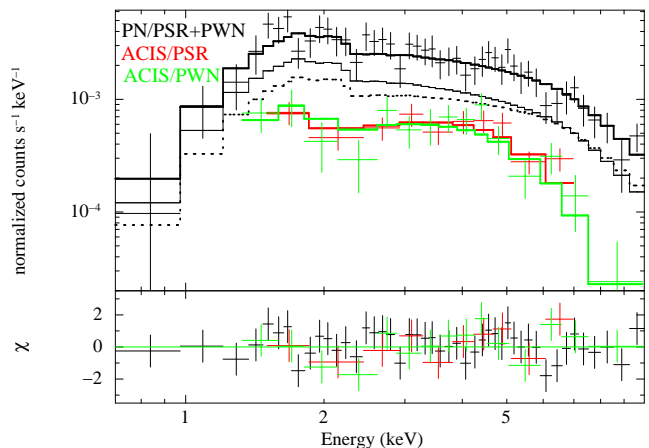


**Figure 2.** Top: Observed X-ray spectra of PSR J1826–1256 and its PWN within 15 arcsec from the pulsar. The data from different instruments and sources are shown by different colours. Bold solid lines show the best-fit models. Dotted and thin solid lines show the pulsar and PWN contribution in the XMM-*Newton* pn-spectrum, respectively. Bottom: Fit residuals.

in Fig. 2. The examples of the PWN spectra from the regions 1 and 4 are shown in Fig. 3.

We also tried to use the BB+PL model for the pulsar, but this did not lead to substantial improvements of the fit statistics: FTEST command provided a probability of about 0.4 that the improvements occurred by chance.

## 4 DISCUSSION

### 4.1 Distance to PSR J1826–1256

To constrain the parameters of the pulsar and its PWN, it is necessary to know the distance.

The only available ‘pseudo’-distance estimate  $D \sim 1.2$  kpc (Marelli 2012) is known to be uncertain within a factor of 2–3. Assuming a 100 per cent efficiency in  $\gamma$ -rays, we obtain  $D \approx 9.4$  kpc. However, this value can be even larger, accounting for an unknown emission beaming factor. Using the pulsar galactic coordinates  $(l, b) = (18.56, -0.38)$

<sup>5</sup> The aperture size was selected using the EREGIONANALYSE tool.

<sup>6</sup> We studied that part of the PWN which is covered by both MOS detectors (in the south-west it is partially projected onto a disabled MOS1 CCD). We did not use *Chandra* data for the nebula spectral analysis due to the gaps between ACIS-I CCDs.

**Table 2.** Best-fitting parameters for the Eel nebula emission (regions 1–6 in Fig. 1). All errors are at 90% confidence. Unabsorbed fluxes  $F_X$  are given in the 0.5–10 keV band.  $N_{\text{bins}}$  = number of spectral bins.

Region	1	2	3	4	5	6
Net counts (MOS1/2)	500/513	435/476	185/239	953/1036	464/479	337/369
Photon index $\Gamma$	$1.34^{+0.18}_{-0.17}$	$1.99^{+0.23}_{-0.22}$	$2.44^{+0.41}_{-0.37}$	$1.76^{+0.16}_{-0.16}$	$2.54^{+0.33}_{-0.31}$	$2.58^{+0.36}_{-0.32}$
PL normalization $K_{\text{PL}}$ , $10^{-5}$ ph s $^{-1}$ cm $^{-2}$ keV $^{-1}$	$2.2^{+0.6}_{-0.5}$	$3.9^{+1.2}_{-0.9}$	$2.7^{+1.2}_{-0.9}$	$6.7^{+1.5}_{-1.2}$	$2.7^{+1.2}_{-0.9}$	$5.5^{+2.2}_{-1.5}$
Flux $F_X$ , $10^{-13}$ erg s $^{-1}$ cm $^{-2}$	$2.07^{+0.16}_{-0.17}$	$1.87^{+0.24}_{-0.19}$	$0.96^{+0.27}_{-0.18}$	$3.99^{+0.34}_{-0.29}$	$2.30^{+0.58}_{-0.38}$	$1.88^{+0.50}_{-0.33}$
Area, arcmin $^2$	1.4	1.5	1.3	3.3	3.0	2.2
Distance from the pulsar, arcmin	1.3	2.2	3.1	3.2	4.0	5.6
$\chi^2(N_{\text{bins}})$	60(63)	46(62)	39(40)	116(128)	81(92)	74(68)

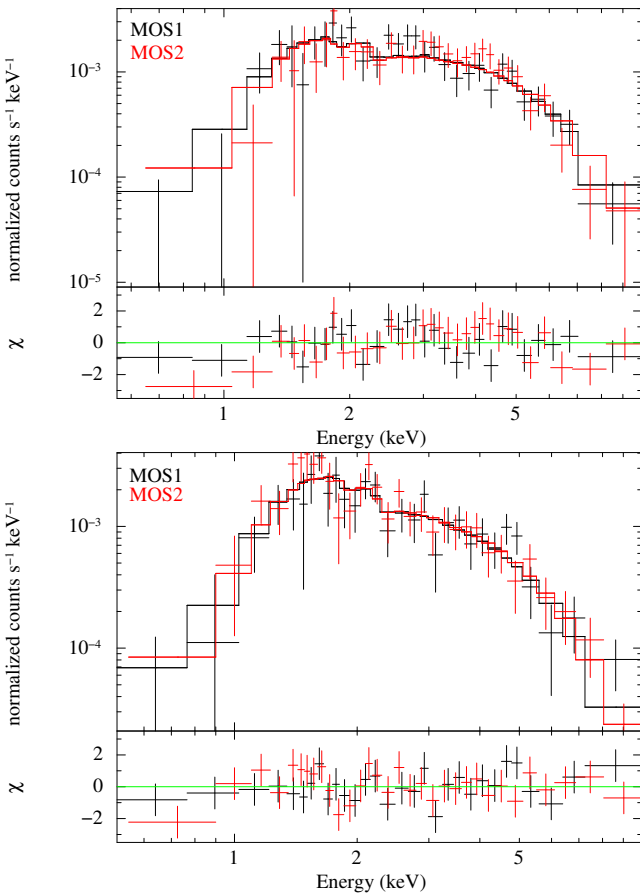


**Figure 3.** Examples of observed X-ray spectra of the Eel nebula extracted from regions 1 (top) and 4 (bottom). The data from different instruments are shown by different colours. Solid lines show the best-fit PL models.

and assuming that it lies inside the Galactic disk with a half-thickness of 100 pc, the maximum  $D$  is  $\sim 15$  kpc if the pulsar is located near the disk edge.

A more reliable distance estimate can be obtained by using the empirical relation between the distance and the interstellar reddening  $E(B - V)$  in the pulsar direction. According to the extinction map by [Schlafly & Finkbeiner](#)

(2011)<sup>7</sup>, the total Galactic  $E(B - V)$  in this direction is about 15.5. The reddening to PSR J1826–1256 can be derived from the column density  $N_{\text{H}}$  value utilizing the relation  $N_{\text{H}} = (8.9 \pm 0.4) \times E(B - V) \times 10^{21}$  cm $^{-2}$  ([Foight et al. 2016](#)).  $N_{\text{H}}$  obtained from the X-ray spectral analysis (Table 1) transforms to  $E(B - V) = 2.45 \pm 0.19$  ( $1\sigma$  errors). This is much smaller than the total Galactic value and implies that the pulsar is much closer than the Galactic disk edge in its direction. We compared the obtained  $E(B - V)$  with the extinction map by [Marshall et al. \(2006\)](#), which is based on Two-Micron All-Sky Survey (2MASS) stars photometry along with the Besançon model of population synthesis. The  $E(B - V)$ –distance relation was constructed using the PYTHON package MWDUST ([Bovy et al. 2016](#)). The resulting  $D$  lies in the range of 3.4–3.6 kpc. This is compatible with the distance estimate of 3 kpc based on the pulsar X-ray luminosity, though such estimate is very uncertain ([Roberts 2009](#)). We adopt 3.5 kpc as a reasonable value in our following estimates.

#### 4.2 Pulsar

The PSR J1826–1256 spectrum can be described by the PL model. The obtained photon index and flux (Table 1) are in agreement with the results of [Marelli \(2012\)](#), who used only *Chandra* data. Addition of the *XMM-Newton* data allowed us to constrain these parameters better. They are different from the results by [Li et al. \(2018\)](#) since they used only the MOS data and did not take into account the PWN contribution in the pulsar aperture.

The pulsar non-thermal X-ray luminosity  $L_X = (1.5 \pm 0.2) \times 10^{32} D_{3.5}^2$  erg s $^{-1}$  and efficiency  $\eta_X = L_X/\dot{E} = (4.2 \pm 0.5) \times 10^{-5} D_{3.5}^2$  in the 0.5–10 keV band, where  $D_{3.5}$  is the distance in the units of 3.5 kpc. The values obtained are typical for pulsars with similar ages and spin-down luminosities, although they are by an order of magnitude higher than those of the Vela pulsar, which is known as a very inefficient non-thermal emitter (e.g., [Kargaltsev & Pavlov 2008](#)). The ratio between the  $\gamma$ -ray ([Marelli 2012](#)) and the non-thermal unabsorbed X-ray fluxes of the pulsar is  $\log(F_\gamma/F_X) \approx 3.5$ . This is in agreement with the value of  $3.5 \pm 0.5$  derived for radio-quiet  $\gamma$ -ray pulsars ([Abdo et al. 2013; Marelli et al. 2015](#)).

<sup>7</sup> <https://irsa.ipac.caltech.edu/applications/DUST/>

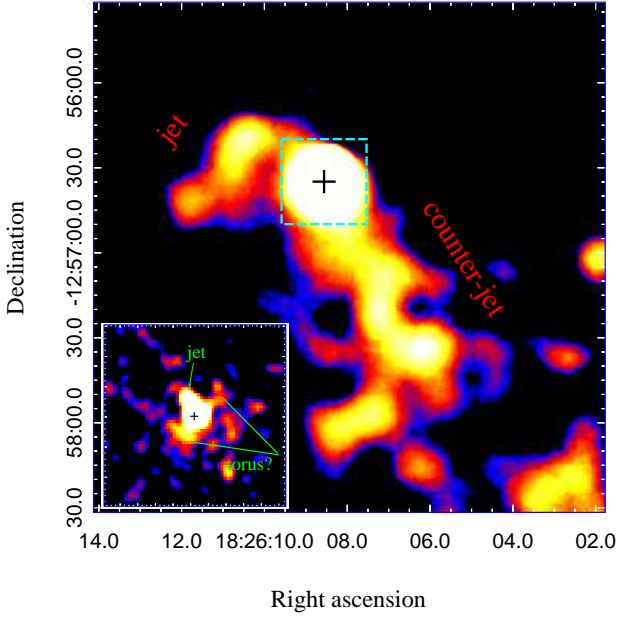


**Figure 4.** 3 arcmin  $\times$  3 arcmin *Chandra* X-ray image of the pulsar vicinity in 0.5–10 keV range smoothed with a 25 pixel Gaussian kernel. The ‘+’ symbol shows the pulsar position. The ‘jet’ and ‘counter-jet’ are marked. The 30 arcsec  $\times$  30 arcsec image part, enclosed by the cyan dashed box and smoothed with a 3 pixel Gaussian kernel, is enlarged in the inset. The possible PWN torus and the base part of the ‘jet’ are marked.

We estimated the PSR J1826–1256 surface temperature adding the BB component to the pulsar non-thermal spectral model and adopting a neutron star (NS) radius of  $13D_{3.5}$  km. We obtained a  $3\sigma$  upper limit on the temperature of  $\approx 0.1$  keV, which is consistent with predictions of standard NS cooling scenarios for a 14 kyr star (Yakovlev & Pethick 2004).

### 4.3 PWN

The spectrum of the PWN within  $\approx 15$  arcsec from the pulsar, with the photon index  $\Gamma = 1.2 \pm 0.2$  (see Table 1), is hard. The same is observed in other PWNe powered by Vela-like pulsars (Bykov et al. 2017). The index increases to  $\approx 2.5$  with the distance from the pulsar (Table 2). Such spectral steepening is observed for some other PWNe and suggests synchrotron cooling (e.g. Reynolds et al. 2017; Slane 2017). The total PWN luminosity is about  $L_X \approx 2 \times 10^{33} D_{3.5}^2$  erg s $^{-1}$ . This corresponds to the X-ray efficiency of  $5.6 \times 10^{-4} D_{3.5}^2$ , which is typical for PWNe.

Roberts (2009) noticed X-ray structures in the pulsar’s near vicinity, which can be interpreted as the PWN torus and jet. By considering the *Chandra* data, we confirm the presence of the presumed torus around the pulsar, with the radius of about 5 arcsec, likely seen edge on, and the north-east jet directed along the torus axis (the insert of Fig. 4). In Fig. 5 we show spatial profiles along these structures, compared with the point spread function (PSF). The latter was generated using CHART (Carter et al. 2003) and MARX tools and the PSR J1826–1256 best-fitting spectral model

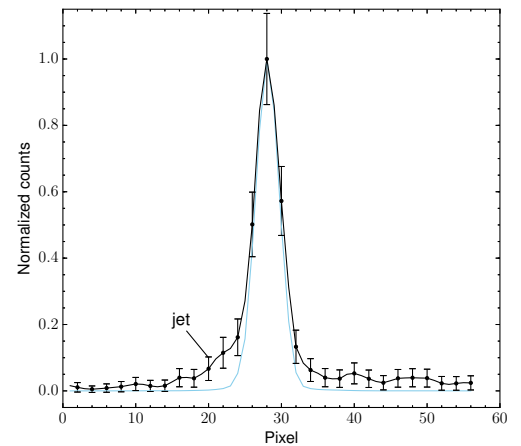
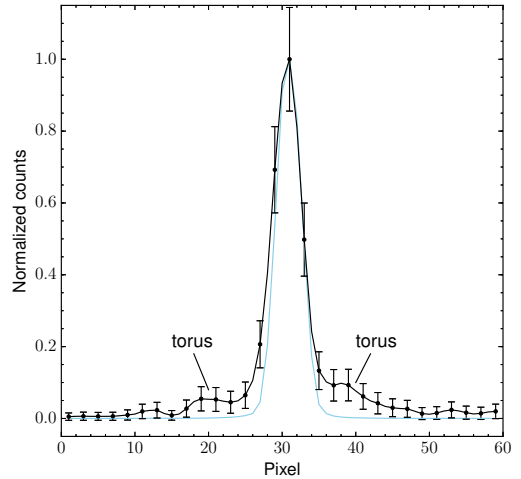
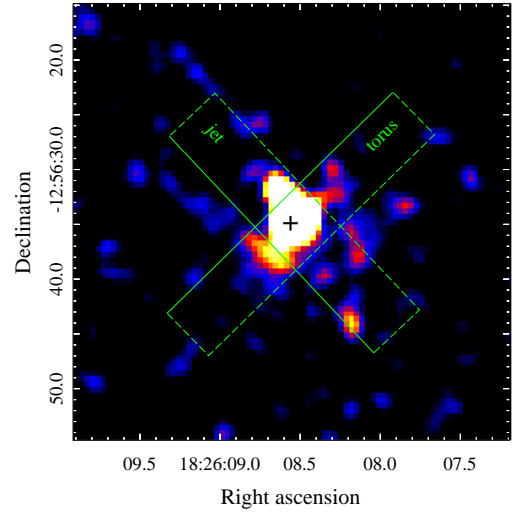


**Figure 5.** *Chandra* X-ray image of the pulsar vicinity in 0.5–10 keV range smoothed with a 3 pixel Gaussian kernel (top). The ‘+’ symbol shows the pulsar position. Green rectangles are used to obtain spatial profiles along the presumed torus and jet structures shown in the middle and bottom panels, respectively. Points (0,0) in horizontal axes correspond to the top-short rectangle sides. The data are shown in black and the PSF – in light-blue. The background level is negligible.

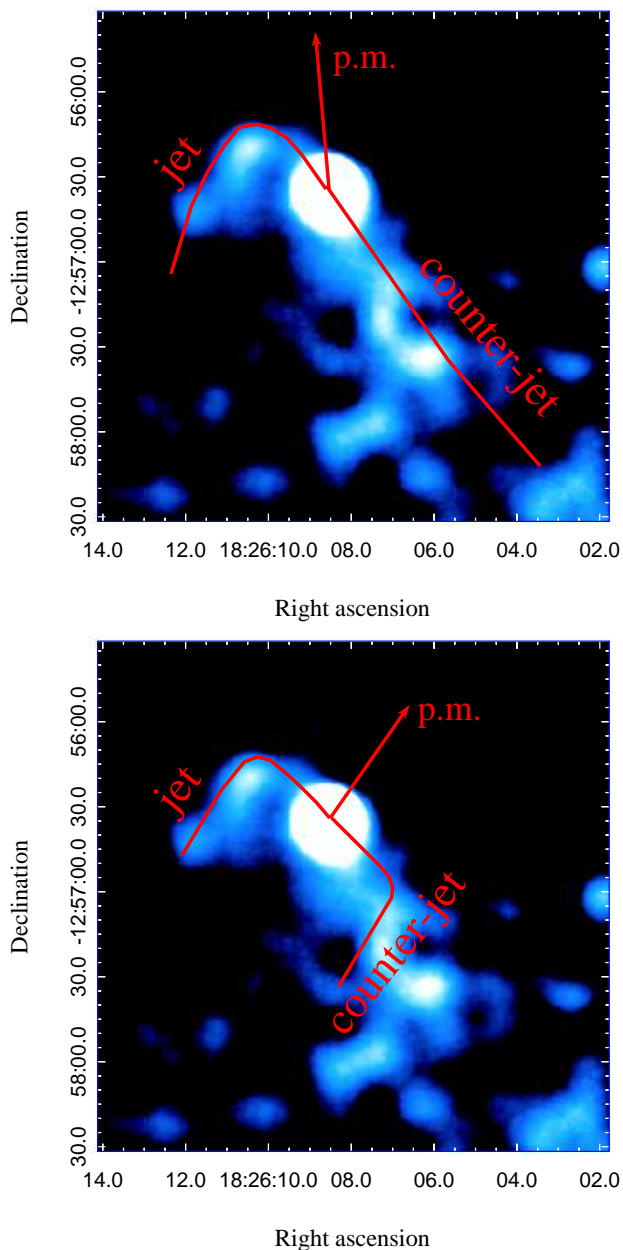


**Figure 6.** The same image as in Fig. 4 but using another color map. Possible geometries of the system are shown by the red lines as suggested in this work (top) and in Kargaltsev et al. (2017) (bottom). Arrows shows the suggested pulsar proper motion (p.m.) directions.

(Table 1)<sup>8</sup>. Emission excesses over the PSF wings corresponding to the torus and jet structures adjacent to the PSF core are clearly seen. Such structures are observed in other young PWNe, including the Vela PWN. In the latter case, the size of the torus is about 2 arcmin (Helfand et al. 2001). At a distance of 3.5 kpc, this would transform to  $\approx 10$  arcsec, which is compatible with the observed dimension of the presumed PSR J1826–1256 torus, suggesting that it is a real PWN structure. Assuming that, we can estimate

the upper limit of the radius of the pulsar wind termination shock (TS) which should be smaller than the torus:  $R_{\text{TS}} \lesssim 2.6 \times 10^{17} D_{3.5}$  cm. This is comparable with that of the Vela PWN ( $5 \times 10^{16}$  cm; Kargaltsev & Pavlov 2008). The respective lower limit on the ambient matter pressure is  $P_{\text{amb}} \approx \dot{E}(4\pi c R_{\text{TS}}^2)^{-1} \approx 0.14 \times 10^{-9} (R_{\text{TS}}/2.6 \times 10^{17} \text{ cm})^{-2} \text{ dyn cm}^{-2}$ . This value is typical for Vela-like pulsars located inside their host SNRs (Kargaltsev et al. 2007). For PSR J1826–1256, this host could be the SNR candidate G18.45–0.42 (see details below).

At a larger scale, we see that the jet mentioned above is bent towards the east, representing the ‘Eel head’ (the main panel of Fig. 4). Roberts (2009) referred it as a ‘forward jet’. The longer ‘Eel body’ extending about 6 arcmin ( $\approx 6D_{3.5}$  pc) south-west of the pulsar can be interpreted as a ‘counter-jet’, which transforms at larger distances to a trail behind the pulsar moving in roughly the opposite direction. The corresponding geometry is shown in the top panel of Fig. 6. The bending of the forward jet could be due to ram pressure if the vector of the pulsar velocity directs approximately to the north. A similar interpretation is considered for the Vela PWN, where the pulsar proper motion and the matter flow initiated by the SNR reverse shock are likely working together to bend the PWN jets (Kargaltsev et al. 2015). To conclude, the Eel appears to be a mixed type morphology PWN containing a torus, jets and a trail.

Note that Kargaltsev et al. (2017) suggested another geometry of the system, which is shown in the bottom panel of Fig. 6 (see also their fig. 6). The corresponding proper motion position angle (P.A.) is  $\sim 330$  deg. However, this geometry cannot describe the long PWN trail. Moreover, only the jet is clearly bent while the counter-jet is not.

#### 4.4 Connection between PSR J1826–1256 PWN, the SNR candidate G18.45–0.42, the open cluster Bica 3 and HESS J1826–130

PSR J1826–1256 and the Eel nebula are located in the complex region containing the SNR candidate G18.45–0.42, the TeV source HESS J1826–130 and the open stellar cluster Bica 3 (Fig. 1). Below we discuss possible associations between them.

It was proposed earlier that HESS J1826–130 is a TeV counterpart to the PSR J1826–1256 PWN (Roberts et al. 2007; Angüner et al. 2017). This suggestion is natural, since there are similar Vela-like systems. One remarkable example is PSR J1823–13 ( $\dot{E} = 2.8 \times 10^{36} \text{ erg s}^{-1}$ ,  $\tau = 21$  kyr; Pavlov, Kargaltsev & Briskin 2008). Measurements of this pulsar’s proper motion allowed authors to understand its connection with HESS J1825–137. Pavlov et al. (2008) suggested that the latter is produced by relic electrons emitted by the pulsar when it was younger and more powerful. Another example is the young and energetic pulsar J1357–6429 ( $\dot{E} = 3.1 \times 10^{36} \text{ erg s}^{-1}$ ,  $\tau = 7.3$  kyr). The pulsar and its PWN are projected onto the extended TeV source HESS J1356–645 (H.E.S.S. Collaboration et al. 2011; Chang et al. 2012). Chang et al. (2012) proposed the most plausible explanation of the TeV and radio emission as arising from a relic PWN.

The Eel-TeV-source association is also supported by the fact that the PWN X-ray and TeV luminosities,  $L_X \approx 2 \times 10^{33} D_{3.5}^2 \text{ erg s}^{-1}$  (this paper) and  $L_\gamma \approx 1.5 \times 10^{33} D_{3.5}^2 \text{ erg s}^{-1}$

<sup>8</sup> For details see <http://cxc.harvard.edu/ciao/PSFs/chart2/index.html>

(H.E.S.S. Collaboration et al. 2018), are consistent with the  $L_{\gamma>\text{TeV}}$  versus  $L_X$  and  $L_{\gamma>\text{TeV}}/L_X$  versus age distributions of other X- $\gamma$ -ray PWNe (Kargaltsev et al. 2013). In addition, if we assume that the TeV source is the relic PWN of J1826 then Bohm diffusion can be the main process of the particle escape and the source expansion. On the time-scale of 14 kyr the particles will diffuse to a distance of  $40B_{-6}^{-1/2}(1+0.144B_{-6}^2)^{-1/2}$  pc, where  $B_{-6}$  is the magnetic field in  $\mu\text{G}$  (Kargaltsev et al. 2013). For the visible TeV source size of about  $9D_{3.5}$  pc, this translates to a magnetic field of about 5  $\mu\text{G}$ , which is a typical value for PWNe.

There is some displacement between the TeV source centres and the pulsars in the systems noticed above, which is usually explained by the effect of the SNR reverse shock on the PWN and/or by the pulsar proper motion (Blondin et al. 2001). The same situation is observed for PSR J1826–1256 and HESS J1826–130 (Fig. 1). Their displacement could be explained naturally by assuming that the SNR candidate G18.45–0.42 is the pulsar host remnant. PSR J1826–1256 is located about 7.5 arcmin off the remnant centre and projects onto its shell (Fig. 1). If the pulsar was born near the G18.45–0.42 centre, for an age of  $\approx 14$  kyr its proper motion has to be  $\approx 32r_{14}^{-1}$  mas yr $^{-1}$ , implying the pulsar transverse velocity of  $\approx 530D_{3.5}$  km s $^{-1}$ . The latter value is consistent with the pulsar velocity distribution (Hobbs et al. 2005). The proper motion P.A. in this case is  $\sim 5$  deg, which is compatible with the geometry explaining the Eel structure presented in the top panel of Fig. 6. The alternative geometry (the bottom panel of Fig. 6) considered by Kargaltsev et al. (2017) raises a question about the PSR J1826–1256 host SNR. In this case, the pulsar cannot be associated with any remnant found around it (Fig. 1).

If G18.45–0.42 is the real SNR related with the pulsar, its observed radius is  $\sim 8D_{3.5}$  pc. At the age of about 14 kyr, it has to be entered into the pressure driven snow-plough phase. Using the SNR evolution code (Leahy & Williams 2017) with typical ISM number density of 0.5–2 cm $^{-3}$  and supernova explosion energy of  $10^{51}$  erg we obtain the blast wave shock radius of about 12–14 pc. Accounting for uncertainties in the age and distance, this is compatible with the observed radius. Deeper study of G18.45–0.42 is necessary to confirm its SNR nature and the association with PSR J1826–1256 and to estimate its distance and age.

We have tried to measure the pulsar proper motion using both *Chandra* observations, providing a time base of 4.4 yr. To perform the astrometric transformation, we used stars detected in both datasets by the WAVDETECT tool with significance  $> 9\sigma$  (sources detected at chips edges were excluded). The short observation was registered to the long one as described in the *Chandra* manual<sup>9</sup>. We obtained only an upper limit on the pulsar position shift of  $\lesssim 0.7$  arcsec corresponding to a non-informative proper motion limit of  $\lesssim 160$  mas yr $^{-1}$  as compared to the expected value of  $\approx 32$  mas yr $^{-1}$  estimated above. There are two reasons for such a rude result. The first one is the short exposure of the *Chandra* observation (ObsID 3851) leading to a non-sufficient signal to noise ratio of  $\approx 6$ . The second is that in this observation the pulsar was exposed at  $\approx 5.5$  arcmin from the telescope aim-point, where the point source localization accuracy degrades

significantly. Additional *Chandra* observations are necessary to measure the proper motion.

The Bica 3 position coincides with the center of G18.45–0.42 which makes it a likely birthplace of this presumed SNR. According to the OPENCLUST catalogue (Dias et al. 2002), the distance to the cluster is about 1.6 kpc. We extracted the cluster spectrum from MOS2 data using the region shown in the bottom right panel of Fig. 1 (in the case of MOS1, Bica 3 is projected on the disabled CCD). It can be described by the absorbed model of collisionally-ionized diffuse gas APEC with column density  $N_{\text{H}} = 7.6_{-1.4}^{+1.7} \times 10^{21}$  cm $^{-2}$  and temperature  $T = 6.3_{-1.5}^{+2.2}$  keV, typical for open clusters (e.g., Skinner et al. 2019).  $N_{\text{H}}$  is about three times lower than the value obtained for PSR J1826–1256 and consistent with the smaller distance to the cluster. Further studies are needed to verify whether G18.45–0.42 is associated with Bica 3 or PSR J1826–1256.

Star clusters can be sources of TeV emission (e.g. Bednarek 2007). However, currently only two open clusters are known to be associated with TeV sources<sup>10</sup>. This makes the direct connection of HESS J1826–130 with Bica 3 unlikely. On the other hand, we can suggest that HESS J1826–130 is the TeV counterpart to G18.45–0.42 basing on their positions and extents.

## 5 SUMMARY

We have analysed the XMM-*Newton* and *Chandra* observations of the young  $\gamma$ -ray radio-quiet pulsar PSR J1826–1256 and its PWN. The pulsar spectrum can be described by the PL model with a photon index  $\Gamma \approx 1$  and the PWN spectrum becomes softer with the distance from the pulsar. We also estimated the distance to PSR J1826–1256 to be  $\approx 3.5$  kpc, using the empirical relation between the distance and interstellar absorption by Marshall et al. (2006).

PSR J1826–1256 can be associated with the recently discovered SNR candidate G18.45–0.42. This implies the pulsar transverse velocity of  $\approx 530D_{3.5}$  km s $^{-1}$ , which is consistent with the pulsars velocity distribution, and the pressure driven snowplough phase of the remnant.

The Eel nebula appears to be a mixed-type morphology PWN containing a torus, jets and a trail. One of the jets is bent by the ram pressure, due to the pulsar proper motion vector not coinciding with the jet direction. Such geometry explains the PWN morphology and supports the association with G18.45–0.42.

The TeV source HESS J1826–130 overlaps with the PSR J1826–1256+PWN system as well as with G18.45–0.42 and the open star cluster Bica 3. Comparing the Eel X-ray and HESS J1826–130  $\gamma$ -ray luminosities with those of other X- $\gamma$ -ray PWNe suggests the TeV source is the relic PWN of PSR J1826–1256. However, we cannot exclude the possibility that G18.45–0.42 can be the HESS J1826–130 counterpart (or partially contribute to TeV emission).

<sup>10</sup> According to the catalog for Very High Energy Gamma-Ray Astronomy (Wakely & Horan 2007); <http://tevcat.uchicago.edu/>. The association of HESS J1848–018 with the star-forming region W43 is in question and it has been also considered as a PWN candidate (Acero et al. 2013).

<sup>9</sup> [http://cxc.harvard.edu/ciao/threads/reproject\\_aspect/](http://cxc.harvard.edu/ciao/threads/reproject_aspect/)



Based on the spatial coincidence of G18.45–0.42 and Bica 3, the latter can be the birthplace for the presumed SNR. The distance estimate to the open cluster is significantly lower than the distance to PSR J1826–1256 which is confirmed by the X-ray spectral analysis. In this case G18.45–0.42 cannot be associated with the pulsar.

The pulsar proper motion measurement is necessary to solve the question about the Eel nebula’s morphological type. Together with confirmation of the G18.45–0.42 SNR nature this can help to understand the relations between the pulsar, G18.45–0.42, HESS J1826–130 and Bica 3.

After this paper submission, the work by [Duvidovich et al. \(2019\)](#) was published. Authors used the same XMM-Newton data to analyse the PSR J1826–1256 and Eel emission. They also found that the spectra of both objects can be described by power laws and the PWN spectrum softens with increasing distance from PSR J1826–1256. They also argued that HESS J1826–130 is likely produced by Eel. However, they did not use Chandra data and performed spectral analysis of only the brightest part of Eel. There are no new distance constraint in their work and they did not discuss the compact nebula morphology and the connections between PSR J1826–1256, G18.45–0.42, HESS J1826–130 and Bica 3.

## ACKNOWLEDGEMENTS

We thank the anonymous referee for useful comments. The work of AVK and DAZ was supported by RF Presidential Programme MK–2566.2017.2. DAZ thanks Pirinem School of Theoretical Physics for hospitality. The work of YAS was supported by the Fundamental Research Program of Presidium of the RAS P-12. The scientific results reported in this article are based on data obtained from the Chandra Data Archive and observations obtained with XMM-Newton, an ESA science mission with instruments and contributions directly funded by ESA Member States and the USA (NASA).

## REFERENCES

- Abdo A. A., et al., 2009, *Science*, **325**, 840  
 Abdo A. A., et al., 2013, *ApJS*, **208**, 17  
 Acero F., et al., 2013, *ApJ*, **773**, 77  
 Acero F., et al., 2015, *ApJS*, **218**, 23  
 Ackermann M., et al., 2011, *ApJ*, **726**, 35  
 Anderson L. D., et al., 2017, *A&A*, **605**, A58  
 Angüner E. O., Casanova S., Oya I., Aharonian F., Bordas P., A. Ziegler for the H. E. S. S. Collaboration 2017, preprint, ([arXiv:1708.04844](#))  
 Bednarek W., 2007, *MNRAS*, **382**, 367  
 Blondin J. M., Chevalier R. A., Frierson D. M., 2001, *ApJ*, **563**, 806  
 Bovy J., Rix H.-W., Green G. M., Schlafly E. F., Finkbeiner D. P., 2016, *ApJ*, **818**, 130  
 Brogan C. L., Gelfand J. D., Gaensler B. M., Kassim N. E., Lazio T. J. W., 2006, *ApJ*, **639**, L25  
 Bykov A. M., Amato E., Petrov A. E., Krassilchtchikov A. M., Levenfish K. P., 2017, *Space Sci. Rev.*, **207**, 235  
 Carter C., Karovska M., Jerius D., Glotfelty K., Beikman S., 2003, in Payne H. E., Jędrzejewski R. I., Hook R. N., eds, *Astronomical Society of the Pacific Conference Series Vol. 295, Astronomical Data Analysis Software and Systems XII*. p. 477  
 Chang C., Pavlov G. G., Kargaltsev O., Shibanov Y. A., 2012, *ApJ*, **744**, 81  
 Dias W. S., Alessi B. S., Moitinho A., Lépine J. R. D., 2002, *A&A*, **389**, 871  
 Duvidovich L., Giacani E., Castelletti G., Petriella A., Supán L., 2019, *A&A*, **623**, A115  
 Foight D. R., Güver T., Özel F., Slane P. O., 2016, *ApJ*, **826**, 66  
 Gaensler B. M., Slane P. O., 2006, *ARA&A*, **44**, 17  
 H.E.S.S. Collaboration et al., 2011, *A&A*, **533**, A103  
 H.E.S.S. Collaboration et al., 2018, *A&A*, **612**, A1  
 Helfand D. J., Gotthelf E. V., Halpern J. P., 2001, *ApJ*, **556**, 380  
 Hobbs G., Lorimer D. R., Lyne A. G., Kramer M., 2005, *MNRAS*, **360**, 974  
 Kargaltsev O., Pavlov G., 2007, *Ap&SS*, **308**, 287  
 Kargaltsev O., Pavlov G. G., 2008, in Bassa C., Wang Z., Cumming A., Kaspi V. M., eds, *American Institute of Physics Conference Series Vol. 983, 40 Years of Pulsars: Millisecond Pulsars, Magnetars and More*. pp 171–185 ([arXiv:0801.2602](#)), [doi:10.1063/1.2900138](#)  
 Kargaltsev O., Pavlov G. G., Garmire G. P., 2007, *ApJ*, **660**, 1413  
 Kargaltsev O., Rangelov B., Pavlov G. G., 2013, preprint, ([arXiv:1305.2552](#))  
 Kargaltsev O., Cerutti B., Lyubarsky Y., Striani E., 2015, *Space Sci. Rev.*, **191**, 391  
 Kargaltsev O., Pavlov G. G., Klingler N., Rangelov B., 2017, *Journal of Plasma Physics*, **83**, 635830501  
 Leahy D. A., Williams J. E., 2017, *AJ*, **153**, 239  
 Li J., Torres D. F., Coti Zelati F., Papitto A., Kerr M., Rea N., 2018, *ApJ*, **868**, L29  
 Marelli M., 2012, PhD thesis, University of Insubria ([arXiv:1205.1748](#))  
 Marelli M., De Luca A., Caraveo P., 2013, *Mem. Soc. Astron. Italiana*, **84**, 568  
 Marelli M., Mignani R. P., De Luca A., Saz Parkinson P. M., Salvetti D., Den Hartog P. R., Wolff M. T., 2015, *ApJ*, **802**, 78  
 Marshall D. J., Robin A. C., Reylé C., Schultheis M., Picaud S., 2006, *A&A*, **453**, 635  
 Pavlov G. G., Kargaltsev O., Brisken W. F., 2008, *ApJ*, **675**, 683  
 Ray P. S., et al., 2011, *ApJS*, **194**, 17  
 Reynolds S. P., Pavlov G. G., Kargaltsev O., Klingler N., Renaud M., Mereghetti S., 2017, *Space Sci. Rev.*, **207**, 175  
 Roberts M. S. E., 2009, *The Pulsar Wind Nebulae of Three Radio Quiet Gamma-Ray Pulsars*, [http://cxc.harvard.edu/cdo/snr09/pres/Roberts\\_Mallory.pdf](http://cxc.harvard.edu/cdo/snr09/pres/Roberts_Mallory.pdf)  
 Roberts M. S. E., Romani R. W., Kawai N., 2001, *ApJS*, **133**, 451  
 Roberts M. S. E., Gotthelf E. V., Halpern J. P., Brogan C. L., Ransom S. M., 2007, in Becker W., Huang H. H., eds, *WE-Heraeus Seminar on Neutron Stars and Pulsars 40 years after the Discovery*. p. 24 ([arXiv:astro-ph/0612631](#))  
 Saz Parkinson P. M., et al., 2010, *ApJ*, **725**, 571  
 Schlafly E. F., Finkbeiner D. P., 2011, *ApJ*, **737**, 103  
 Skinner S. L., Sokal K. R., Güdel M., 2019, *ApJ*, **871**, 116  
 Slane P., 2017, *Pulsar Wind Nebulae*. p. 2159, [doi:10.1007/978-3-319-21846-5\\_95](#)  
 Snowden S. L., Kuntz K. D., 2014, *Cookbook for analysis procedures for XMM-Newton EPIC observations of extended objects and the diffuse background*. <http://heasarc.gsfc.nasa.gov/docs/xmm/esas/cookbook>  
 Takata J., Cheng K. S., 2017, *ApJ*, **834**, 4  
 Viganò D., Rea N., Pons J. A., Perna R., Aguilera D. N., Miralles J. A., 2013, *MNRAS*, **434**, 123  
 Wakely S. P., Horan D., 2007, in *Proceedings of the 30th International Cosmic Ray Conference (ICRC 2007): Merida, Yucatan, Mexico, July 3-11, 2007*. pp 1341–1344, <http://indico.nucleares.unam.mx/contributionDisplay.py?contribId=5>  
 Wilms J., Allen A., McCray R., 2000, *ApJ*, **542**, 914  
 Yakovlev D. G., Pethick C. J., 2004, *ARA&A*, **42**, 169

This paper has been typeset from a  $\text{T}_{\text{E}}\text{X}/\text{L}^{\text{A}}\text{T}_{\text{E}}\text{X}$  file prepared by the author.